

Electrical conductivity in extremely disordered molybdenum oxynitrides thin films

J. A. Hofer,^{1*} S. Bengio,² G. Rozas,^{1,2} P. D. Pérez,² M. Sirena,^{1,2} S. Suárez,^{1,2} N. Haberkorn.^{1,2}

¹ *Instituto Balseiro, Universidad Nacional de Cuyo and Comisión Nacional de Energía Atómica, Av. Bustillo 9500, 8400 San Carlos de Bariloche, Argentina.*

² *Comisión Nacional de Energía Atómica and Consejo Nacional de Investigaciones Científicas y Técnicas, Centro Atómico Bariloche, Av. Bustillo 9500, 8400 San Carlos de Bariloche, Argentina.*

We report on the influence of the chemical composition on the electronic properties of molybdenum oxynitrides thin films grown by reactive sputtering on Si (100) substrates at room temperature. The partial pressure of Ar was fixed at 90 %, and the remaining 10 % was adjusted with mixtures N₂:O₂ (varying from pure N₂ to pure O₂). The crystalline and electronic structures and the electrical transport of the films depend on the chemical composition. Thin films grown using oxygen mixtures up 2 % have γ -Mo₂N phase and display superconductivity. The superconducting critical temperature T_c reduces from ~ 6.8 K to below 3.0 K as the oxygen increases. On the other hand, films grown using oxygen mixtures richer than 2 % are mostly amorphous. The electrical transport shows a semiconductor-like behavior with variable-range hopping conduction at low temperatures. The analysis of the optical properties reveals that the samples have not a defined semiconductor band gap, which can be related to the high structural disorder and the excitation of electrons in a wide range of energies.

Keywords: molybdenum; oxynitrides; thin films; sputtering; electrical transport.

Email: juan.hofer@cab.cnea.gov.ar

1. Introduction

The structural, mechanical and electronic properties of ceramics usually depend on the doping level and the type of anions. For oxynitrides, the oxidation state of the cations, the bond covalence and the band structure can be tuned by mixing oxygen and nitrogen. The wide range of electronic and optical properties make them promising candidates for photocatalysis [1,2], electronic [3,4,5] and solar energy applications [6]. Depending on the potential application, the study of the physical properties of metallic oxynitrides usually is performed in nanoparticles [7] and in thin films [8]. In addition to the doping, the properties of the materials are also affected by the microstructure. Among the chemical and physical methods for the fabrication of thin films, sputtering has the advantage that it is possible to obtain from amorphous to epitaxial structures by modifying the substrate temperature.

From an electronic point of view, it is interesting to study the role of the oxygen doping on the properties of superconducting nitrides. For materials such as TiN [9] and NbN [10], the structural and electrical properties can be tuned adding oxygen and other dopant elements [11,12]. For example, adding oxygen a crossover from a dirty superconducting nitride (due to paramagnetic oxygen impurities) to a semiconductor oxynitride can be expected [13]. Among the candidates to analyze the effect of stoichiometry on the electrical and structural properties are molybdenum oxynitrides. The most common molybdenum oxides are the monoclinic dioxide (MoO_2) and the trioxide (MoO_3). MoO_2 exhibits unusual properties among oxides, shifting from one with metallic properties into a semiconductor when the structural disorder increases. [14,15, 16,17]. MoO_3 is *n*-type semiconductor [18]. On the other hand, molybdenum nitrides present several superconducting crystalline phases: γ - Mo_2N (cubic) with a superconducting critical temperature $T_c \sim 5$ K [19], β - Mo_2N (tetragonal) with $T_c \sim 5$ K [20] and δ - MoN (hexagonal) with $T_c \sim 12$ K [21,22]. The chemical composition of molybdenum nitride thin films grown by reactive sputtering can be adjusted by the gas mixture [23]. A distinctive property of γ - Mo_2N thin films is that its T_c rises from ≈ 5 K to 8 K as the disorder at the nanoscale increases [24,25]. Notwithstanding the rich properties displayed by the nitrides and oxides, there are only a few studies on the electrical properties of molybdenum oxynitrides [26,27].

In this work, we analyze the influence of the reactive gas mixture on the structural, chemical and electronic properties of molybdenum oxynitrides thin films grown at room temperature by reactive sputtering on Si (100) substrates. The reactive atmosphere is

an Ar:N₂:O₂ mixture. The Ar: (N₂+O₂) ratio was fixed in 90:10 and the N₂:O₂ ratio varied from 0 to 10. The results show that the microstructure and electrical properties depend on the gas mixture. Nitrogen-rich films are superconducting and the T_c is gradually reduced by increasing the oxygen doping. Oxygen-rich films display a semiconductor-like behavior. The physical properties of the samples are analyzed by considering the influence of the chemical doping and of the structural disorder.

2. Material and methods

Molybdenum oxynitride films were deposited by DC reactive magnetron sputtering on Si (100) (typical size 1 cm²). No intentional heating of the substrate was used. The base pressure in the chamber was 1.3x10⁻⁴ Pa. Films were grown from a pure Mo target (diameter 3.3 cm) in a reactive Ar:N₂:O₂ mixture. The target power was fixed at 50 W and the total pressure in 0.67 Pa. The substrate was positioned directly over the target at ≈ 5.5 cm. Reactive sputtering was performed with 90% Ar and 10 % of a N₂:O₂ mixture (with O₂ total fraction 0, 1%, 2%, 3.3%, 5%, 6.6% and 10%). The notation [MoN_xO_y] indicates thin films growth in a N₂:O₂ gas mixture where x and y are the respective percentages.

X-ray (XRD) diffraction data was obtained using a Panalytical Empyrean equipment operated at 40 kV and 30 mA with the Cu_{Kα} radiation. The structural analysis was performed based on Θ -2 Θ scans with an angular resolution of 0.02°. The film thickness was measured by low-angle X-ray reflectivity (XRR). AFM measurements were performed in a Dimension 3100 ©Brucker microscope. The AFM images presented in this work were performed in tapping mode. The chemical stoichiometry of the films was analyzed by Rutherford Backscattering Spectroscopy (RBS) with a TANDEM (NEC, 1.7 MV) accelerator using a 2 MeV ⁴He²⁺ ion beam. Surface composition analysis was performed by X-ray photoelectron spectroscopy (XPS) using a standard Al/Mg twin-anode X-ray gun and a hemispherical electrostatic electron energy analyzer (high vacuum conditions with a base pressure of 10⁻⁹Torr).

The optical parameters of for [MoN_{6.6}O_{3.3}], [MoN_{3.3}O_{6.6}], and [MoN₀O₁₀] were deduced from spectroscopic ellipsometry measurements (Ψ and Δ) carried out in the spectral region of 200–1200 nm using a Woollam NIR-Vis-UV ellipsometer in three different angles of incidence: 61°, 66° and 71°. The data was analyzed using the manufacturer's

code. The electrical transport measurements were performed using the standard four-point configuration.

3. Results and discussion

The thicknesses of the films were determined from XRR. The modulation in the Θ - 2Θ scans is related to the thickness d of the film as:

$$\sin^2\theta = \left[\frac{(n+k)\lambda}{2d}\right]^2 + 2\delta, \quad [1]$$

where $1-\delta$ is the real part of the index of refraction of the film, and $k = 0$ (intensity minimum) and $k = \frac{1}{2}$ (intensity maximum) [28]. Figure 1a shows $\sin^2\theta - vs - n^2$ for the low angle minima for films grown for 5 minutes using different gas mixtures. Inset Fig. 1a shows the XRR data for $[\text{MoN}_{10}\text{O}_0]$. Figure 1b shows a summary of the total thickness. The results indicate that the growth rate using Ar: N_2 is 16 nm/ min (see Inset Fig.1b). The value rises with a clear crossover at $\approx 2\%$ O_2 as the oxygen in the mixture increases. Finally, the growth rate for $\approx 10\%$ O_2 (no N_2) is 28 nm/min. The analysis of the surface topology indicates that is weakly affected by the gas mixture. Figure 2 shows AFM images for the extremes $[\text{MoN}_{10}\text{O}_0]$ and $[\text{MoN}_0\text{O}_{10}]$. The films display very smooth surfaces with Root Mean Square (RMS) roughness smaller than 0.5 nm.

Figure 3 shows the XRD patterns for molybdenum oxynitride films. Nitrogen-rich films display reflections corresponding to the $\gamma\text{-Mo}_2\text{N}$ phase [23]. For pure N_2 and low O_2 concentrations, the films are textured along the (200). The reflections (111) and (200) are observed in $[\text{MoN}_8\text{O}_2]$. Gas mixtures richer than 2 % in O_2 produce mainly amorphous films, which is evident from the absence of peaks in the XRD patterns. The change in the microstructure from nanocrystalline Mo_2N phase to an amorphous phase is coherent with the increment in the growth rate described earlier. To understand about the influence of the stoichiometry on the structural changes, we study the chemical composition by RBS. Table 1 shows a summary of the results. The error bar for the data is 5 %. The extremes $[\text{MoN}_{10}\text{O}_0]$ and $[\text{MoN}_0\text{O}_{10}]$ correspond to $\text{Mo}_2\text{N}_{1.1}$ and MoO_2 , respectively. The data show that for gas mixtures with oxygen above 2% the stoichiometry of nitrogen drops and the samples are mainly oxides. This crossover in

the chemical composition is in agreement with the presence of amorphous structures in the XRD data.

XPS analysis was employed to investigate the electronic structure of the pristine and cleaned films. The surface cleaning was performed with Ar⁺ sputtering (2 kV). The pristine films display a component at binding energy (BE) \approx 232.7 eV related to superficial MoO₃ that is removed during the sputtering process [29]. Figure 4 shows the XPS spectra in the Mo3d region for cleaned [MoN₁₀O₀], [MoN₈O₂], [MoN₅O₅] and [MoN₀O₁₀]. The results can be divided into nitrides and oxides. The spectra for cleaned [MoN₁₀O₀], and [MoN₈O₂], display the Mo₂N component (binding energy BE \approx 228.5 eV) shifted to smaller BE by 0.2 eV (see Fig. 4a). The electronic structure for oxygen mixtures richer than 2 % displays the MoO₂ with BE \approx 229.3 eV (not shown). After clean the surface, [MoN₅O₅] and [MoN₀O₁₀] suffer a drastic reduction showing MoO and metallic Mo (see Fig.4b) [30,31,32].

To understand in more detail the electronic structure of the films, we analyzed its valence band spectra. Figure 5 shows a summary of the results. The comparison between [MoN₁₀O₀] and [MoN₈O₂] indicates that for the same contribution of N2s, the first displays a higher O2s intensity (see Fig. 5a). [MoN₈O₂] displays a larger contribution of the metallic Mo4d. The latter is also observed at [MoN₅O₅] and [MoN₀O₁₀] (see Fig. 5b). The contribution of N drops as the oxygen increases. It is important to note that nitrides are more stables than oxides to the sputtering process [33]. No nitrogen vacancies are formed during the sputtering process used to clean the surface in [MoN₁₀O₀]. While oxygen vacancies are formed in [MoN₅O₅] and [MoN₀O₁₀]. The spectrum for [MoN₈O₂] suggests that the sample is affected by the creation of oxygen and presumably nitrogen vacancies. This supposition explains the shift in the shift in the Mo3d spectra and the rise in the Mo4d intensity relative to the O1s and N1s. Furthermore, the width of the Mo4d peak and its proximity to the N2p orbital reveals a high hybridization (see top panel Fig. 5), while the narrow Mo4d peak and its distancing with the O2p orbital indicate lower hybridization (see bottom panel Fig. 5).

To correlate the microstructure and the electronic properties, we measured the electrical resistivity versus temperature for the different films (see Fig. 6). The results show that films with reactive mixtures with O₂ up 2% display superconductivity. The T_c decreases from \approx 6.8 K for [MoN₁₀O₀] to \approx 3 K for [MoN₈O₂]. Thin films grown using oxygen mixtures above 3.3 % display a semiconductor-like behavior. The measured resistivity at 273 K was found to $\rho^{273\text{ K}} = 100$ (20) $\mu\Omega\cdot\text{cm}$ for [MoN₁₀O₀], 140 (20) $\mu\Omega\cdot\text{cm}$ for [MoN₉O₁], 180 (20) $\mu\Omega\cdot\text{cm}$ for [MoN₈O₂], 200 (20) $\mu\Omega\cdot\text{cm}$ for [MoN_{6.6}O_{3.3}], 250 (20)

$\mu\Omega\cdot\text{cm}$ for $[\text{MoN}_5\text{O}_5]$, 700 (20) $\mu\Omega\cdot\text{cm}$ for $[\text{MoN}_{3.3}\text{O}_{6.6}]$, and 1500 (50) $\mu\Omega\cdot\text{cm}$ for $[\text{MoN}_0\text{O}_{10}]$,

Following, the influence of the oxygen impurities in the superconducting properties is analyzed by measuring the upper critical field (H_{c2}). The temperature dependence of H_{c2} for dirty superconductors is described by the Werthamer-Helfand-Hohenberg (WHH) formula [34]:

$$\ln \frac{1}{t} = \sum_{\nu=-\infty}^{\infty} \left(\frac{1}{|2\nu+1|} - \left[|2\nu+1| + \frac{\hbar}{t} + \frac{(\alpha\hbar/t)^2}{|2\nu+1|+(\hbar+\lambda_{so})/t} \right]^{-1} \right), \quad [2]$$

where $t = T / T_c$, $\hbar = (4/\pi^2)(H_{c2}(T)/|dH_{c2}/dT|_{T_c})$, α is the Maki parameter, and λ_{so} is the spin-orbit scattering constant. When $\lambda_{so} = 0$, $H_{c2}(0)$ obtained from the WHH formula

satisfies the relation $H_{c2}(0) = \frac{H_{c2}^{orb}(0)}{\sqrt{1+\alpha^2}}$ [35]. Figure 7 shows the summary of the results.

The inset in Fig. 7 shows typical curves of normalized resistance versus temperature for different magnetic fields in $[\text{MoN}_9\text{O}_1]$. The experimental data is well described by the WHH model using $\alpha = 0$ and $\lambda_{so} = 0$ (see dashed lines in Fig. 7). The obtained $H_{c2}(0)$ values are 12 T for $[\text{MoN}_{10}\text{O}_0]$, 9 T for $[\text{MoN}_9\text{O}_1]$ and 6 T for $[\text{MoN}_8\text{O}_2]$. The coherence length $\xi(0)$ values can be estimated using $\xi(0) = \sqrt{\Phi_0 / (2\pi H_{c2}^{\parallel}(0))}$ (with $\Phi_0 = 2.07 \times 10^{-7} \text{ G cm}^2$ is the flux quantum). The obtained $\xi(0)$ values are 5.2 nm for $[\text{MoN}_{10}\text{O}_0]$, 6 nm for $[\text{MoN}_9\text{O}_1]$ and 7.4 for $[\text{MoN}_8\text{O}_2]$. It is important to note that for a weakly coupled BCS superconductor with similar band structure $\xi_0 = 0.18 \frac{\hbar v_F}{k_B T_c}$ (v_F : Fermi velocity and k_B

the Boltzmann constant) [36]. The $\xi_0 * T_c$ value for the different films decreases as the oxygen increases, which suggests modifications in the band structure.

Now we will analyze the semiconductor-like behavior for $[\text{MoN}_5\text{O}_5]$, $[\text{MoN}_{3.3}\text{O}_{6.6}]$, and $[\text{MoN}_0\text{O}_{10}]$ in more detail. In general, the temperature dependence of the resistivity in disordered systems and amorphous semiconductors takes the following form:

$$\rho \approx \rho_0 \exp \left[- \left(\frac{T_0}{T} \right)^p \right], \quad [3]$$

where ρ_0 is a prefactor, T_0 is a characteristic temperature and the exponent p depends on the shape of the density of states at the Fermi level (FL) [37]. For Mott variable range hopping (VHR) p can be $1/4$ (3D systems) or $1/3$ (2D systems). Moreover, $p = 1/2$ is expected for 2D systems in which the Coulomb interaction is important. Figure 8 shows $\ln(\rho)$ vs. $T^{-1/4}$ for the analyzed samples. Straight lines are observed at low temperatures. To verify 3D VRH at low temperatures with $p = 1/4$, the equation [3] can

be rewritten as $W = -\frac{\delta(\ln\sigma(T))}{\delta(\ln T)} = p(T/T_0)^p$ [38]. Inset Fig. 8 shows

$\ln W$ versus $\ln T$ for $[\text{MoN}_{3.3}\text{O}_{6.6}]$, the slope $p = 0.24$ (0.01) confirms the mechanism. The T_0 values obtained from the slopes are 1.4 K, 4.5 K and 25 K, for $[\text{MoN}_5\text{O}_5]$, $[\text{MoN}_{3.3}\text{O}_{6.6}]$, and $[\text{MoN}_0\text{O}_{10}]$, respectively. From the values of T_0 it is possible to estimate the hopping energy $E_h(T)$ for a given temperature T [39]:

$$E_h(T) = \frac{1}{4}k_B T^{3/4} T_0^{1/4}. \quad [4]$$

The E_h (5 K) goes from 10 μeV to 160 μeV when the oxygen is increased. These values are much smaller than those usually observed for more insulating samples such as manganites and ZnO [39,40].

The semiconductor-like behavior in the samples was analyzed by ellipsometry measurements. Refractive index (n) and extinction coefficient (k) were calculated from the modeling of the ellipsometric variables (Ψ and Δ). Figure 9a shows the results for wave lengths λ between 200 nm and 1200 nm for $[\text{MoN}_5\text{O}_5]$, $[\text{MoN}_{3.3}\text{O}_{6.6}]$ and $[\text{MoN}_0\text{O}_{10}]$. The refraction index increases monotonically as the energy decreases. Moreover, $K(\lambda)$ is different from the dependence expected for semiconductors with a defined band gap. There is not a crossover to lower absorption when the energy decreases. For amorphous semiconductors, there is not long range atomic order. However, the short-range order remains to some extent, giving rise thereby to a band-like structure of electron energy states similar to that of crystalline semiconductors. Nevertheless, the absorption edge becomes indistinguishable due to the high disorder. Electrons in the called diffuse band can contribute to the conduction even for low energies. To verify the presence of a gap when the disorder is reduced, $[\text{MoN}_0\text{O}_{10}]$ was annealed at 600 °C for 1 hour using a vacuum of 1.3×10^{-4} Pa (sample 1) and 101325 Pa O_2 (sample 2). Figure 9b shows the $n(\lambda)$ and the $K(\lambda)$ dependences after annealing. The latter displays a strong decrease in the visible and near-infrared (NIR) range in agreement with the expectations for semiconductors. In the case of the oxygen-annealed sample, we cannot estimate reliable optical properties because the small absorption and thickness of the annealed material difficult the fitting of the ellipsometric optical model. In fact, the obtained n and k values are greatly influenced by the optical properties of the Si substrate. For the vacuum-annealed sample, however, we can estimate a band gap using an $(\alpha h\nu)^2$ vs. $(h\nu)$ plot (with $\alpha = 4\pi k/\lambda$) [16,41]. Inset Fig. 9b shows the obtained results for annealed $[\text{MoN}_0\text{O}_{10}]$. Two different band gaps can be identified. The presence of defined gaps indicates that the thermal

annealing increases the order and reduces the contribution of the called diffuse band. The film annealed in vacuum display energy gap values of 2.15 eV and 2.74 eV. The values are in the range of those previously reported for MoO₂ and MoO₃ [16[41]. The presence of two gaps in the samples may be related to disorder and changes in oxygen stoichiometry. Similar features have been previously observed in thermal annealed Mo oxide thin films obtained by electrodeposition [16].

4. Conclusions

In summary, we analyzed the influence of the chemical composition on the electronic properties of molybdenum oxynitrides thin films grown by reactive sputtering on Si (100) substrates at room temperature. The electronic properties of the films are affected by the composition of the reactive gas mixture. For rich N₂, the films are superconducting. The T_c is systematically reduced from ≈ 6.8 K for Mo-64 at.% N-36 at.% to ≈ 3 K for Mo-53 at.%N-30 at.% O-17 at.%. The oxygen is an interstitial impurity in the superconducting γ -Mo₂N phase and is also segregated as amorphous MoO₂. For rich O₂ mixtures, the films are mainly amorphous oxide and display a semiconductor-like behavior. The electrical resistivity depends on the oxygen content. The electrical transport shows a semiconductor-like behavior with a VRH conduction at low temperatures. The analysis of the optical properties reveals that the samples have not a defined semiconductor band gap, which can be related to the high disorder and the excitation of electrons in a wide range of energies. The presence of a semiconductor gap is evidenced for annealed samples. Further investigations on the influence of the thermal annealing on the electronic should contribute to understand the role of the disorder on the resulting electronic properties.

Acknowledgments

This work was partially supported by the ANPCYT (PICT 2015-2171), U. N. de Cuyo 06/C505 and CONICET PIP 2015-0100575CO. JAH, SBM, GR, MS and NH are members of the of the Instituto de Nanociencia y Nanotecnología, CNEA-CONICET.

Declarations of interest: none.

Table 1. Chemical composition (atomic (%)) obtained from RBS measurements. The error bars for the data are estimated in approximately 5 %.

Figure 1. a) $\sin^2\theta - vs - n^2$ for the minima in the XRR data. Solid line is the least-squares linear fit to the data. Inset: typical XRR data for $[\text{MoN}_{10}\text{O}_0]$. b) Thickness for films grown during 5 minutes using different gas mixtures. The data is calculated from the slope of a). Inset: Growth rate for the different gas mixtures.

Figure 2. AFM topographical images ($10 \times 10 \mu\text{m}^2$) of $[\text{MoN}_{10}\text{O}_0]$ (left) and $[\text{MoN}_0\text{O}_{10}]$ (right).

Figure 3. XRD for cleaned molybdenum oxynitride films.

Figure 4. XPS Mo3d spectra for $[\text{MoN}_{10}\text{O}_0]$, $[\text{MoN}_8\text{O}_2]$, $[\text{MoN}_5\text{O}_5]$ and $[\text{MoN}_0\text{O}_{10}]$.

Figure 5. XPS valence band spectra for surface cleaned $[\text{MoN}_{10}\text{O}_0]$, $[\text{MoN}_8\text{O}_2]$, $[\text{MoN}_5\text{O}_5]$ and $[\text{MoN}_0\text{O}_{10}]$. Inset shows the spectra for pristine $[\text{MoN}_5\text{O}_5]$ and $[\text{MoN}_0\text{O}_{10}]$.

Figure 6. a) Electrical resistivity versus temperature for molybdenum oxynitride films grown using different gas mixtures. b) Normalized resistance vs. temperature at $T < 10$ K for superconducting samples. c) Summary of T_c versus oxygen concentration in the reactive mixture.

Figure 7. Temperature dependence of the upper critical field (H_{c2}) for $[\text{MoN}_{10}\text{O}_0]$, $[\text{MoN}_9\text{O}_1]$ and $[\text{MoN}_8\text{O}_2]$. Inset shows typical curves of the resistance for different applied magnetic fields for $[\text{MoN}_9\text{O}_1]$.

Figure 8. $\ln \rho$ vs $T^{1/4}$ for $[\text{MoN}_5\text{O}_5]$, $[\text{MoN}_{3.3}\text{O}_{6.6}]$ and $[\text{MoN}_0\text{O}_{10}]$. The inset shows $\ln W$ vs $\ln T$ for $[\text{MoN}_{3.3}\text{O}_{6.6}]$ (with $W = -\frac{\delta(\ln\sigma(T))}{\delta(\ln T)}$).

Figure 9. Wavelength dependence of the refractive index (n) and extinction coefficient (k) of: a) as-deposited $[\text{MoN}_5\text{O}_5]$, $[\text{MoN}_{3.3}\text{O}_{6.6}]$ and $[\text{MoN}_0\text{O}_{10}]$; b) $[\text{MoN}_0\text{O}_{10}]$ annealed at 600 °C in vacuum and under 101325 Pa O_2 . Inset shows $(\alpha h\nu)^2$ vs. $h\nu$ curves for vacuum-annealed $[\text{MoN}_0\text{O}_{10}]$.

Figure 1.

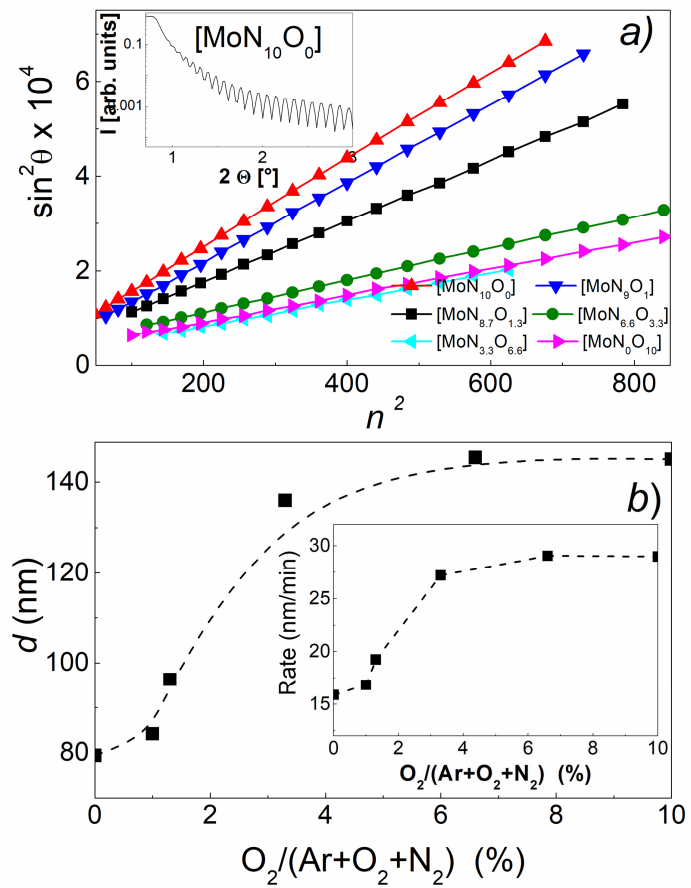


Figure 2.

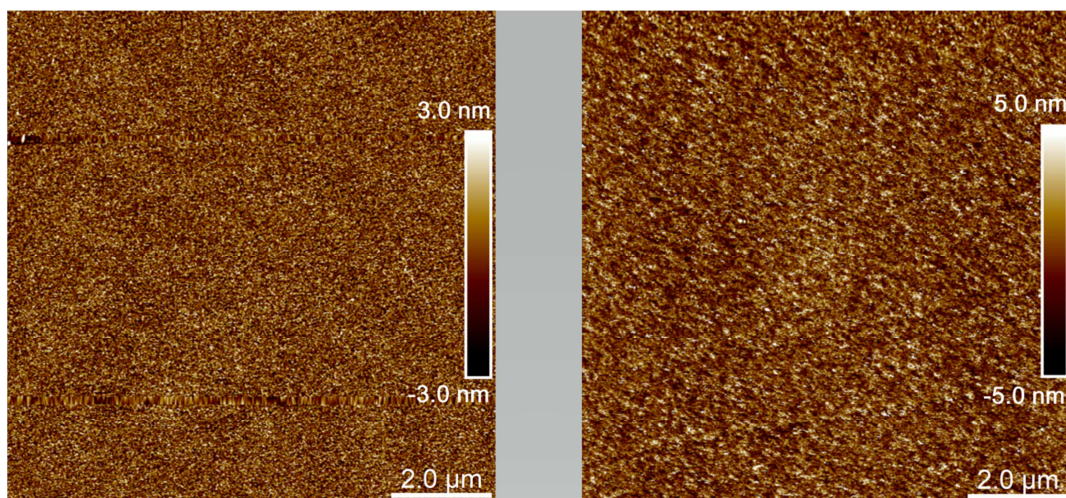


Figure 3.

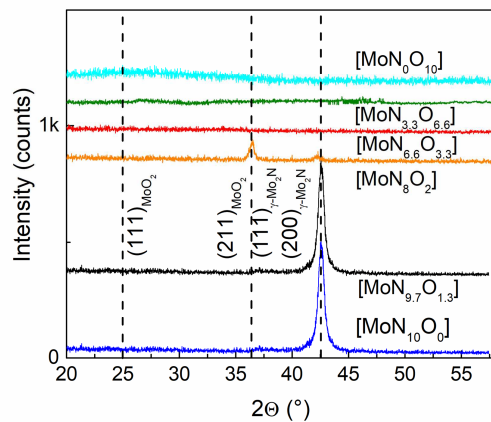


Figure 4.

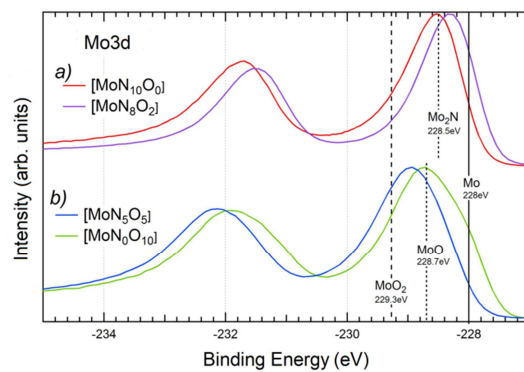


Figure 5.

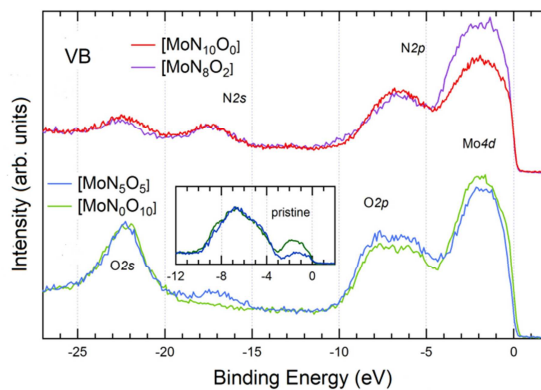


Figure 6.

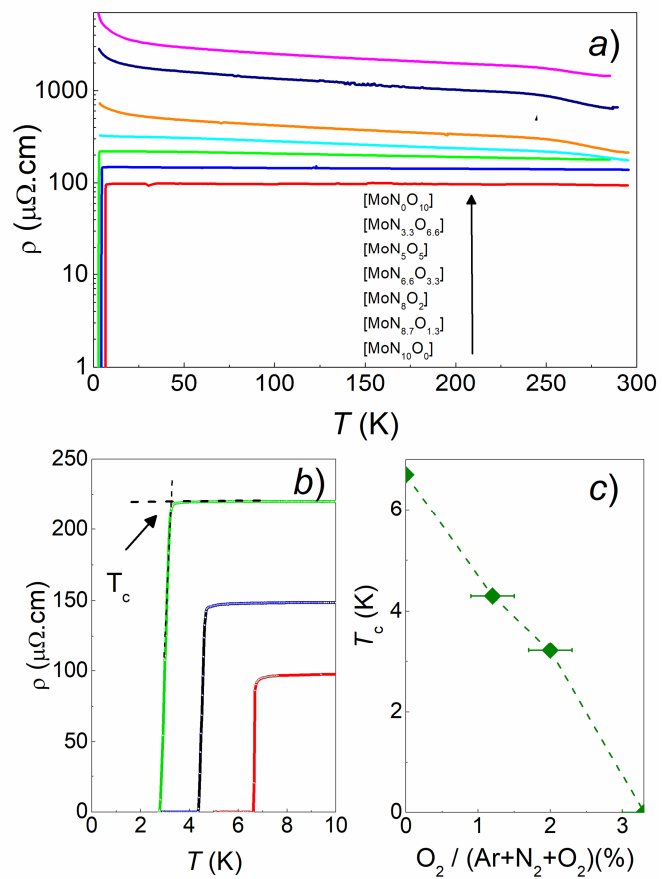


Figure 7.

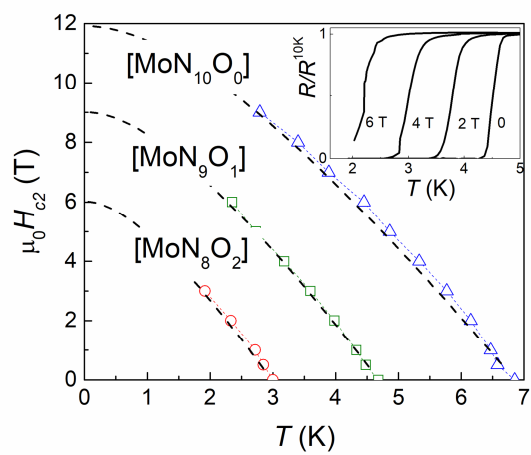


Figure 8.

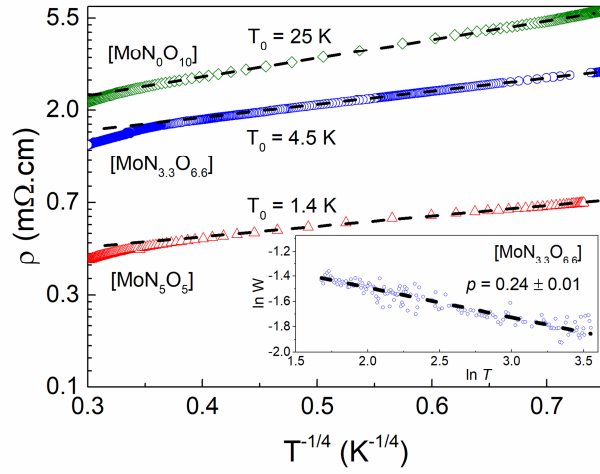


Figure 9.

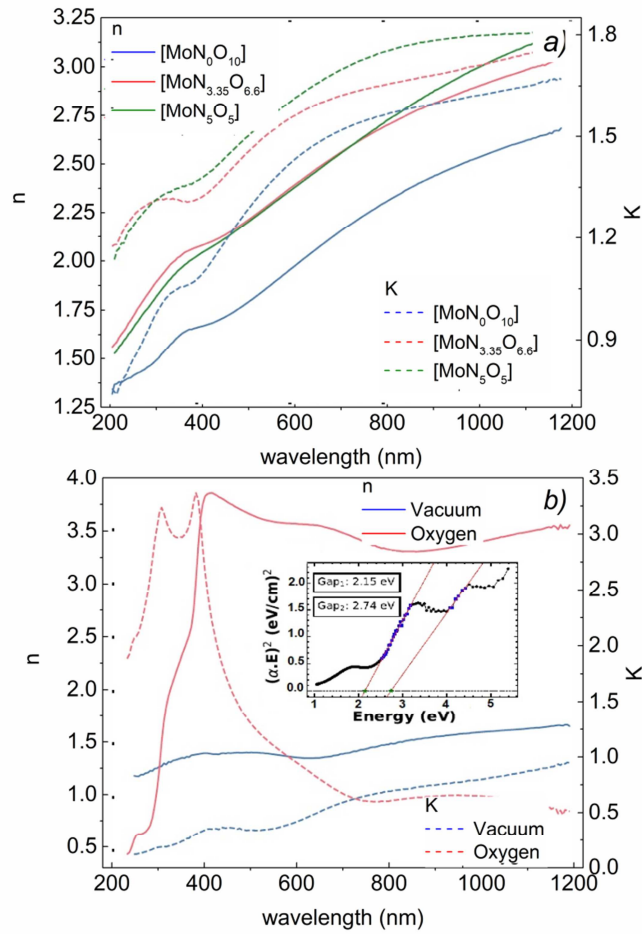


Table I.

Sample	Mo	N	O
[MoN ₁₀ O ₀]	0.64	0.36	--
[MoN ₉ O ₁]	0.54	0.34	0.12
[MoN ₈ O ₂]	0.53	0.3	0.17
[MoN _{6.6} O _{3.3}]	0.34	0.26	0.40
[MoN ₅ O ₅]	0.40	0.24	0.36
[MoN _{3.3} O _{6.6}]	0.40	0.24	0.35
[MoN ₀ O ₁₀]	0.33	--	0.67

- [1] R. Kikuchi, T. Kouzaki, T. Kurabuchi, K. Hato, Characterization of baddeleyite-structure NbON films deposited by RF reactive sputtering for solar hydrogen production devices, **83** *Electrochemistry* (2015) 711-714. <https://doi.org/10.5796/electrochemistry.83.711>
- [2] Mitsuharu Chisaka, Yuta Ando, Yusuke Yamamoto, Noriaki Itagaki, A Carbon-Support-Free Titanium Oxynitride Catalyst for Proton Exchange Membrane Fuel Cell Cathodes, *Electrochim. Acta* **214** (2016) 165-172. <https://doi.org/10.1016/j.electacta.2016.08.032>
- [3] R.-J Xie, N. Hirosaki, Silicon-based oxynitride and nitride phosphors for white LEDs-A review, *Sci. Technol. Adv. Mater.* **8** (2007) 588–600. <https://doi.org/10.1016/j.stam.2007.08.005>
- [4] C. Le Paven *et al.* Ferroelectric and dielectric study of strontium tantalum based perovskite oxynitride films deposited by reactive rf magnetron sputtering, *Mat. Res. Bull* **96** (2017) 126-132. <https://doi.org/10.1016/j.materresbull.2016.11.030>
- [5] Melita Sluban *et al.* Controlling Disorder and Superconductivity in Titanium Oxynitride Nanoribbons with Anion Exchange, *ACS Nano* **9** (2015) 10133–10141. <https://doi.org/10.1021/acs.nano.5b03742>
- [6] M. Ahmed, G. Xinxin, A review of metal oxynitrides for photocatalysis, *Inorg. Chem. Front.* **3** (2016) 578-590. <https://doi.org/10.1039/C5QI00202H>
- [7] Yusuke Asakura, Yoshiyuki Inaguma, Koichiro Ueda, Yuji Masubuchi, Shu Yin, Synthesis of gallium oxynitride nanoparticles through hydrothermal reaction in the presence of acetylene black and their photocatalytic NO_x decomposition, *Nanoscale* **10** (2018) 1837-1844. <https://doi.org/10.1039/C7NR07502B>
- [8] Laurentiu Braic, Nikolaos Vasilantonakis, Andrei Mihai, Ignacio Jose Villar Garcia, Sarah Fearn, Bin Zou, Neil McN. Alford, Brock Doiron, Rupert F. Oulton, Stefan A. Maier, Anatoly V. Zayats, Peter K. Petrov, Titanium Oxynitride Thin Films with Tunable Double Epsilon-Near-Zero Behavior for Nanophotonic Applications, *ACS Appl. Mater. Interfaces* **9** (2017) 29857–29862. <https://doi.org/10.1021/acsami.7b07660>
- [9] Y Igasaki, H. Mitsuhashi, The effects of substrate bias on the structural and electrical properties of TiN films prepared by reactive r.f. sputtering, *Thin Solid Films* **70** (1978) 17-25. [https://doi.org/10.1016/0040-6090\(80\)90407-1](https://doi.org/10.1016/0040-6090(80)90407-1)
- [10] D. W. Deis, J. R. Gavaler, J. K. Hulm, C.K. Jones, High field properties of pure niobium nitride thin films, *J. Appl. Phys.* **40** (1969) 2153-2156. <https://doi.org/10.1063/1.1657941>
- [11] Melita Sluban, Polona Umek, Zvonko Jagličić, Jože Buh, Petra Šmitek, Aleš Mrzel, Carla Bittencourt, Peter Guttman, Marie-Helene Delville, Dragan Mihailović, and Denis Arčon. Controlling Disorder and Superconductivity in Titanium Oxynitride Nanoribbons with Anion Exchange, *ACS Nano* **9** (2015) 10133–10141. <https://doi.org/10.1021/acs.nano.5b03742>

- [12] Teruki Motohashi, Masahiko Ito, Yuji Masubuchi, Makoto Wakeshima, Shinichi Kikkawa, Crystal Structure and Superconducting Properties of Hexagonal Lithium–Niobium Oxynitride, *Inorg. Chem.* **51** (2012) 11184–11189. <https://doi.org/10.1021/ic301870n>
- [13] Tamer S. El-Shazly, Walid M. Hassan, Sayed S. Abd-el-Rehim; Nageh K. Allam, Optical and electronic properties of niobium oxynitrides with various N/O ratios: insights from first-principles calculations, *J. Photon. Energy* **8** (2018) 026501. <https://doi.org/10.1117/1.JPE.8.02650>
- [14] Yifeng Shi, Bingkun Guo, Serena A. Corr, Qihui Shi, Yong-Sheng Hu, Kevin R. Heier, Liquan Chen, Ram Seshadri, Galen D. Stucky, Ordered Mesoporous Metallic MoO₂ Materials with Highly Reversible Lithium Storage Capacity, *Nano Lett.* **9** (2009) 4215–4220. <https://doi.org/10.1021/nl902423a>
- [15] K. Inzani, M. Nematollahi, F. Vullum-Bruer, T. Grande, T. W. Reenaasb, S. M. Selbach. Electronic properties of reduced molybdenum oxides, *Phys. Chem. Chem. Phys.* **19** (2017) 9232–9245. <https://doi.org/10.1039/C7CP00644F>
- [16] R. S. Patil, M. D. Uplane, P. S. Patil, Structural and optical properties of electrodeposited molybdenum oxide thin films, *Appl. Surf. Sci.* **252** (2006) 8050–8056. <https://doi.org/10.1016/j.apsusc.2005.10.016>
- [17] Zhong Cheng Xiang, Qin Zhang, Zhong Zhang, Xi Jin Xua Qing Bao Wang, Preparation and photoelectric properties of semiconductor MoO₂ micro/nanospheres with wide bandgap. *Ceram. Intern.* **41** (2015) 977–981 <https://doi.org/10.1016/j.ceramint.2014.09.017>.
- [18] Isabela Alves de Castro, Robi Shankar Datta, Jian Zhen Ou, Andres Castellanos-Gomez, Sharath Sriram, Torben Daeneke, Kourosh Kalantar-zadeh, Molybdenum Oxides – From Fundamentals to Functionality, *Adv. Mater* **29** (2017) 1701619. <https://doi.org/10.1002/adma.201701619>
- [19] B. T. Matthias, J. K. Hulm, A Search for New Superconducting Compounds, *Phys. Rev.* **87** (1952) 799–806. <https://doi.org/10.1103/PhysRev.87.799>.
- [20] Kei Inumaru, Kazuya Baba, Shoji Yamanaka, Synthesis and Characterization of Superconducting β -Mo₂N Crystalline Phase on a Si Substrate: An Application of Pulsed Laser Deposition to Nitride Chemistry, *Chem. Mater.* **17** (2005) 5935–5940. <https://doi.org/10.1021/cm050708i>.
- [21] Shanmin Wang, Daniel Antonio, Xiaohui Yu, Jianzhong Zhang, Andrew L. Cornelius, Duanwei He, Yusheng Zhao, The Hardest Superconducting Metal Nitride, *Scient. Rep.* **5** (2015) 13733. <https://doi.org/10.1038/srep13733>.
- [22] Hanlu Zhang *et al.*, Self-assembled *c*-axis oriented δ -MoN thin films on Si substrates by chemical solution deposition: Growth, transport and superconducting, *J Alloys Compd* **704** (2017) 453–458. <https://doi.org/10.1016/j.jallcom.2017.02.084>
- [23] N. Haberkorn, S. Bengio, S. Suárez, P. D. Pérez, M. Sirena, J. Guimpel, Effect of the nitrogen-argon gas mixtures on the superconductivity properties of reactively sputtered molybdenum nitride thin films, *Mater. Lett* **215** (2018) 15–18. <https://doi.org/10.1016/j.matlet.2017.12.045>
- [24] R. Baskaran, A. V. Thanikai Arasu, E. P. Amaladass, L. S. Vaidhyanathan, D. K. Baisnab, Increased upper critical field for nanocrystalline MoN thin films deposited on AlN buffered substrates at ambient temperature, *J. Phys. D* **49** (2016) 205304–205307. <https://doi.org/10.1088/0022-3727/49/20/205304>.
- [25] N. Haberkorn, S. Bengio, S. Suárez, P. D. Pérez, J. A. Hofer, M. Sirena, Effect of thermal annealing and irradiation damage on the superconducting critical temperature of nanocrystalline γ -Mo₂N thin films, *Mater Lett.* **236** (2019) 252–255. <https://doi.org/10.1016/j.matlet.2018.10.094>.
- [26] Juyun Park, Yong-Cheol Kang, Surface characterization of Mo oxynitride films obtained by RF sputtering at various N₂ ratios, *Met. Mater. Int.* **19** (2013) 55–60. <https://doi.org/10.1007/s12540-013-1010-9>.
- [27] Dan Ruan, Rui Lin, Kui Jiang, Xiang Yu, Yaofeng Zhu, Yaqin Fu, Zilong Wang, He Yan, Wenjie Mai, High-Performance Porous Molybdenum Oxynitride Based Fiber Supercapacitors, *ACS Appl. Mater. Interfaces* **9** (2017) 29699–29706. <https://doi.org/10.1021/acsami.7b07522>
- [28] O. Nakamura, Eric E. Fullerton, J. Guimpel, Ivan K. Schuller. High T_c thin films with roughness smaller than one unit cell, *Appl. Phys. Lett* **60** (1992) 120–122. <https://doi.org/10.1063/1.107343>.
- [29] N. Haberkorn, S. Bengio, H. Troiani, S. Suárez, P. D. Perez, P. Granell, F. Golmar, M. Sirena, J. Guimpel, Thickness dependence of the superconducting properties of γ -Mo₂N thin

- films on Si (001) grown by DC sputtering at room temperature, *Mater Chem Phys.* **204** (2018) 48-57. <https://doi.org/10.1016/j.matchemphys.2017.10.015>.
- [30] Geug-Tae Kim, Tae-Keun Park, Hongsuk Chung, Young-Tae Kim, Moo-Hyun Kwon, Jeong-Gil Choi, Growth and characterization of chloronitroaniline crystals for optical parametric oscillators: I. XPS study of Mo-based compounds, *Appl. Surf. Sci.* **152** (1999) 35-43. [https://doi.org/10.1016/S0169-4332\(99\)00293-7](https://doi.org/10.1016/S0169-4332(99)00293-7).
- [31] Jonas Baltrusaitis, Beatriz Mendoza-Sanchez, Vincent Fernandez, Rick Veenstrab, Nijole Dukstiene, Adam Roberts, Neal Fairley, Generalized molybdenum oxide surface chemical state XPS determination via informed amorphous sample model, *Appl. Surf. Sci.* **326** (2015) 151–161. <https://doi.org/10.1016/j.apsusc.2014.11.077>.
- [32] D. O. Scanlon, Graeme W. Watson, D. J. Payne, G. R. Atkinson, R. G. Egdell, and D. S. L. Law. Theoretical and Experimental Study of the Electronic Structures of MoO₃ and MoO₂. *J. Phys. Chem C* **114** (2010) 4636-4645. <https://doi.org/10.1021/jp9093172>
- [33] Z. B. Zhaobin Wei, P. Grange, B. Delmon, XPS and XRD studies of fresh and sulfided Mo₂N, *Appl. Surf. Sci.* **135** (1998) 107-114. DOI: 10.1016/S0169-4332(98)00267-0
- [34] N.R. Werthamer, E. Helfand, P.C. Hohenberg, Temperature and purity dependence of the superconducting critical field, H_{c2}. III, Electron Spin Spin-Orbit Effects, *Phys. Rev.* **147** (1966) 295-302. <https://doi.org/10.1103/PhysRev.147.295>
- [35] K. Maki, Effect of Pauli Paramagnetism on Magnetic Properties of High-Field Superconductors, *Phys. Rev.* **148** (1966) 362-369. <https://doi.org/10.1103/PhysRev.148.362>
- [36] Tinkham, M. Introduction to Superconductivity 2nd edn (McGraw-Hill, 1996).
- [37] I. S. Beloborodov, A. V. Lopatin, V. M. Vinokur, K. B. Efetov, *Rev Mod Phys.* **79** (2007) 469-518. <https://doi.org/10.1103/RevModPhys.79.469>
- [38] Chiashain Chuang, R.K.Puddy, Huang-De Lin, Shun-Tsung Lo, T.-M.Chen, C.G. Smith, C.-T. Liang, Experimental evidence for Efros–Shklovskii variable range hopping in hydrogenated grapheme, *Solid State Comm.* **152** (2012) 905-908. <https://doi.org/10.1016/j.ssc.2012.02.002>
- [39] S. Ravi, M. Kar, Study of magneto-resistivity in La_{1-x}Ag_xMnO₃ compounds, *Physica B: Cond. Matter* **348** (2004) 169-176. <https://doi.org/10.1016/j.physb.2003.11.087>
- [40] Yung-Lung Huang, Shao-Pin Chiu, Zhi-Xin Zhu, Zhi-Qing Li, Juhn-Jong Lin, Variable-range-hopping conduction processes in oxygen deficient polycrystalline ZnO films. *J. Appl. Phys.* **107** (2010) 063715. <https://doi.org/10.1063/1.3357376>
- [41] Tarsame S. Sian, G.B. Reddy, Optical, structural and photoelectron spectroscopic studies on amorphous and crystalline molybdenum oxide thin films, *Sol. Energy Mater. Sol. Cells* **82** (2004) 375–386. <https://doi.org/10.1016/j.solmat.2003.12.007>.